

Correlating experiment and theory for electron paramagnetic resonance and substrate binding in a lytic polysaccharide monooxygenase

Yusuf A. Theibich,[†] Stephan P. A. Sauer,[†] Leila Lo Leggio,[†] and Erik D.

Hedegård^{*,‡}

[†]*Department of Chemistry, University of Copenhagen*

[‡]*Division of Theoretical Chemistry, Lund University, Chemical Centre, P. O. Box 124,
SE-221 00 Lund*

E-mail: erik.hedegard@teokem.lu.se

Abstract

Lytic polysaccharide monooxygenases (LPMOs) are enzymes that binds polysaccharides followed by an (oxidative) disruption of the polysaccharide surface, thereby boosting depolymerization. The binding process between LPMO and polysaccharide is key to the mechanism and recent investigations have established structure-function relationships for this binding, employing hyperfine coupling constants (HFCs) from EPR spectroscopy. Unfortunately, EPR does not provide direct structural data and therefore the experimental EPR parameters have been supported with parameters calculated with density functional theory. Yet, calculated HFCs are extremely sensitive to the employed computational setup. Using the LPMO *Ls*(AA9)A, we here quantify the importance of several choices in the computational setup, ranging from the use of specialized basis, the underlying structures, and the employed exchange–correlation functional. We compare our results to both X-ray structures and experiment (EPR

spectra) for *Ls*(AA9)A as well as to recent experimental/theoretical results for another (AA10) family of LPMOs.

Introduction

The discovery of new copper enzymes boosting depolymerization of polysaccharides,^{1,2} has further fueled the hope of exploiting the vast carbon resource of naturally occurring (but mostly recalcitrant) polysaccharides.³ An obvious utilization is biofuel production but also commercial chemicals would be a rewarding target. The enzymes responsible for the boost belong to a family of auxiliary activity⁴ (AA) enzymes and are denoted lytic polysaccharide monooxygenases (LPMOs).^{1,2} Their auxiliary activity is associated with oxidation of the glycoside link in polysaccharides² leading to disruption of the (crystalline) polysaccharide surface with concomitant boost in polysaccharide decomposition.⁵ A number of different

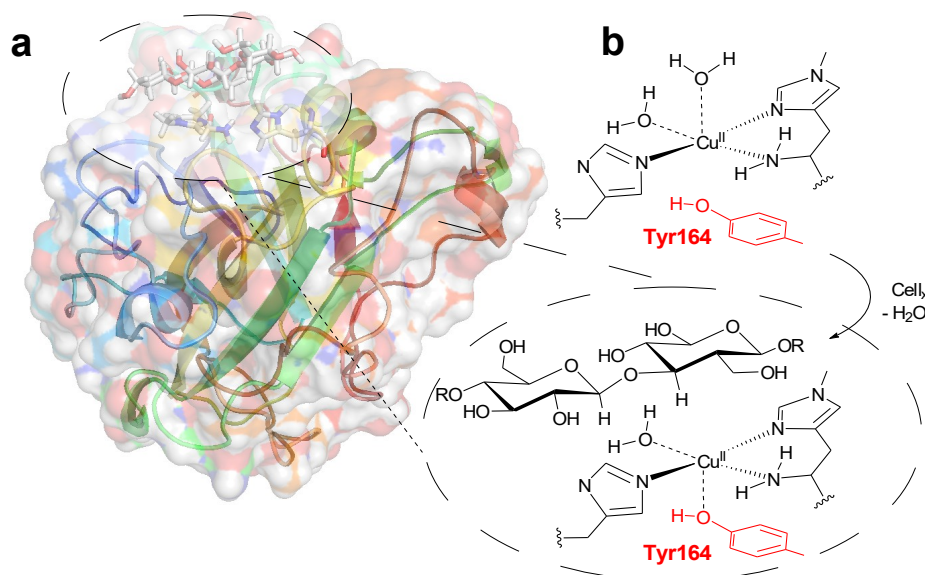


Figure 1: (a) Structure of *Ls*(AA9)A (PDB: 5ACF) with substrate bound.⁶ (b) The histidine brace without substrate and the postulated changes occurring when a substrate binds (displacement of water and tighter binding of Tyr164).

LPMOs have been categorized, belonging to the distinct classes, AA9–AA16 (with AA12 exempted).^{1,2,7–13} The overall structures of the LPMOs are similar, although amino-acid sequences for the different LPMO families vary considerably; they also target a wide range

of different polysaccharide substrates.^{14–17} The most important common feature is the overall fold, a large, flat substrate-binding surface, and an active site with a copper ion⁷, coordinated by two histidine residues (see Figure 1). This motif has become known as the histidine brace, in which one histidine is the amino-terminal residue that coordinates bidentate through the N-terminus and the imidazole side chain.

The mechanism behind LPMOs’ remarkable reactivity is still heavily debated. For instance, the nature of the species responsible for oxidation of the glycoside link is not clarified.^{18–28} The co-substrate is also debated as both O_2 and H_2O_2 have been suggested as the natural co-substrate.^{29,30} Another crucial part of the mechanism is the initial substrate binding on the LPMO surface. The LPMOs generally target insoluble polysaccharide substrates, making study of the binding a large challenge, requiring both different techniques as well as theoretical models. On the experimental side, site-directed mutagenesis^{1,31,32} has been employed to single out important amino acids on the binding surface. The binding process has also been studied directly by nuclear magnetic resonance (NMR)^{33,34} although it is often necessary to resort to Zn-loaded or apo-proteins since copper can obscure the spectra.

Complementary information to NMR can be obtained with electron paramagnetic resonance (EPR) in the Cu(II) state: The different LPMO families usually exhibit EPR spectra characteristic of so-called type 2 copper sites.³⁵ In type 2 copper sites, the (axially) distorted structures give g-values over 2, a pattern with $g_z > g_x \approx g_y$, and hyperfine coupling tensors with large A_z values ($A_z > A_x \approx A_y$). An exception is the EPR spectra of AA10 LPMOs: while they may still be considered axial, AA10 EPR spectra display substantial broadening and more rhombicity (i.e. different g- and A-tensor values) than other LPMOs.³⁶ Data for AA11–AA15 LPMOs are more sparse and occasionally ambiguous,^{12,37} but can generally also be considered as type 2 copper sites.

Employing EPR, geometrical and electronic structures changes have been linked to the substrate binding process,^{38–41} through spectral perturbations on substrate addition: Borisova et al.³⁸ obtained increased g_z and $|A_z|$ -values after adding substrate to an AA9

LPMO. Similar changes have been observed in other studies^{39,42} and have been associated with displacement of an axial water molecule and tighter binding of axial tyrosine.³⁹ Perturbation of EPR spectra upon substrate addition was also recently reported for the AA10 LPMO*Sm*AA10A.⁴⁰ Although not all LPMOs display these perturbations,^{7,11,36} the observed changes of the EPR spectra have been interpreted to indicate a change in electronic structure that prepare the active site for interaction with an exogenous ligand (e.g O₂ or H₂O₂).³⁹ This point has further been elaborated in an integrated NMR and EPR study, suggesting that substrate binding and O₂ activation mechanisms are coupled.⁴³

In several of the recent investigations,^{40,43} experimental EPR spectra were complemented by spin-Hamiltonian parameters calculated by density functional theory (DFT), thus providing an interesting new angle to the study of LPMO substrate binding. Theoretical studies of the binding process have otherwise mainly been carried out using (classical) molecular dynamics (MD) or docking.^{34,38,44,45} Calculation of EPR parameters have previously been applied to blue copper proteins^{46,47} and can perhaps also provide new evidence for changes associated to substrate binding for LPMOs. Still, it is well known (as also stressed in Refs. 40 and 43) that calculated EPR parameters are extremely sensitive to the computational setup.^{48–56} Here we will therefore quantify the sensitivity of calculated EPR parameters to typical choices made in the computational setup: we investigate the role of the underlying structure, i.e., the size of the model used to represent the active site and whether relaxing a larger part of the surrounding protein during structure optimization has an effect. We additionally investigate to what extent specialized basis sets are required and how large the effect of the employed DFT functional is. Our focus is here on Cu(II) hyperfine couplings (HFCs) and ligand (super) HFCs. We target the AA9 LPMO *Ls*(AA9)A since for this system we can compare both calculated QM/MM structures, and EPR parameters with experimental counterparts.³⁹ Finally, our study can also indicate if results from AA10 LPMOs^{40,43} are transferable to AA9 LPMOs.

Computational details

QM/MM structure optimizations

The employed structures for the active site were constructed from QM/MM optimizations based on the LPMO–substrate complex crystal structure of *Ls*(AA9)A³⁹ (PDB 5ACF). For both the substrate-bound complex and the LPMO without substrate, we have in most cases employed structures obtained previously^{27,57} and we refer to these studies for more explicit details regarding the optimizations (a few structures were optimized for this work, but the setup was identical to the ones presented in Refs. 27,57). All structure optimizations were performed with an electrostatic embedded QM/MM approach, using the QM software Turbomole 7.1⁵⁸ and the MM software AMBER 14.⁵⁹ The QM/MM calculations were performed with the COMQUM interface,^{60,61} which combines these two programs. The QM/MM optimizations employed DFT as QM method in form of dispersion corrected TPSS-D3^{62,63} with Becke–Johnson damping⁶⁴ together with a def2-SV(P) basis set.^{65,66} Additional optimizations were also carried out with the def2-TZVPD basis set. The protein was described with the Amber FF14SB force field⁶⁷ and water molecules with the TIP3P model.⁶⁸ When the substrate was included in the MM part, it was described by the glycam.v06 force field.⁶⁹ The optimizations were carried out with both MM region frozen and with residues within 6 Å of the QM region structurally relaxed (at the MM level). The QM system is comprised of Cu, the first coordination sphere and parts of the substrate (see Figure 2). We use the labels “free” and “fixed” for calculations with the MM system fixed or partly relaxed, respectively. Note that all QM/MM optimizations were performed without second-sphere His147 and Gln162 residues in the QM region (which were included in most of our earlier studies,^{27,57} as they are involved directly in the mechanisms investigated).

For the optimizations without substrate, the substrate was removed and the protein re-equilibrated (with identical procedure as described in Refs. 27,57,70), allowing a water molecule to bind to the solvent-exposed active site. The structures were then QM/MM

optimized with an active site identical (apart from the substrate) to the optimizations with substrate. A slight difference from Ref. 57 (apart from that the residues Gln162 and His147 were not included) is that both "fixed" and "free" optimizations were performed for this work. We use "fixed" to indicate an structurally unrelaxed MM region, while "free" indicates that all residues within 6 Å of the QM region are structurally relaxed at the MM level.

EPR parameter calculations

From fixed and free QM/MM optimizations, respectively, we cut out three different sizes of systems on which calculations of EPR parameters were carried out. The different models are shown in Figure 2. We calculate both HFCs of Cu and coordinating N atoms. For Cu, the isotropic Fermi contact term, the anisotropic spin-dipolar contribution, as well as the spin-orbit coupling contributions were calculated. The contributions from spin-orbit coupling are often non-negligible for Cu,^{49,52,71,72} but increase the computational effort considerably: they are calculated as a linear response function of the paramagnetic spin-orbit and the spin-orbit coupling operators. This is also why small models are required for the larger basis sets. Spin-orbit coupling can safely be neglected for the super HFCs of the nitrogen atoms and here only the two first-order terms were evaluated. Basis set studies as well as studies on structures with fixed QM/MM region were only carried out on model 1.

The calculations of the EPR hyperfine and super hyperfine coupling constants were carried out with the ORCA program version 4.1.1.^{49,51,73,74} Before investigating model 1–3 with a range of functionals, we investigated the use of specialized core-property basis sets. For this basis set study, we grouped the atoms in five groups, in short Cu/{N&O_{Eq}&O_{Tyr}}/{C_{Im}&N_{Im}}/C/H (see Figure 2). Thus, the Cu atom is the first group. In the second group the nitrogen and oxygen atoms coordinating the Cu atom were included. The third group consists of the carbon and other nitrogen atoms in the imidazole rings, while the fourth group includes all other carbon atoms. All hydrogen atoms, finally, constitute the fifth group. We then employed the specialized core-property basis set aug-cc-pVTZ-J^{75–80} either

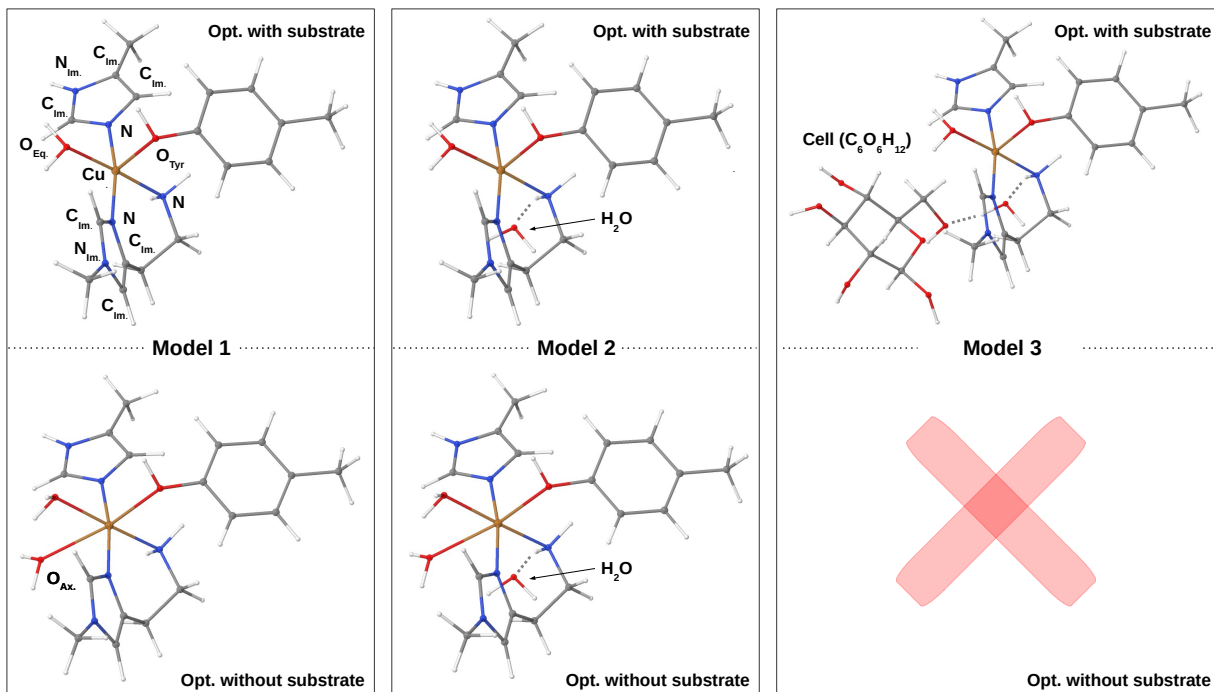


Figure 2: Different model sizes in the study of EPR parameters; all are based on QM/MM optimizations with slightly larger QM regions (cf. the SI) and the MM regions relaxed. For model 1 an additional set of structures were obtained from QM/MM optimizations with MM region unrelaxed. The differences between the models are highlighted with labels (model 1 optimized with substrate also shows labels used for the basis set study).

on all atoms or only on some atoms in a locally-dense basis set fashion^{81–85} together with the standard correlation consistent basis sets cc-pVDZ, cc-pVTZ and aug-cc-pVTZ^{86–88} on the other atoms. Denoting the basis sets aug-cc-pVTZ-J, aug-cc-pVTZ, cc-pVTZ and cc-pVDZ as aTJ, aT, T and D, we obtain a series of six basis sets, systematically decreasing in size: B6 (aTJ/aTJ/aTJ/aTJ/aTJ), B5 (aTJ/aTJ/aTJ/aTJ/D), B4 (aTJ/aTJ/aTJ/aTJ/D), B3 (aTJ/aTJ/aTJ/T/D), B2 (aTJ/aTJ/T/T/D), B1 (aTJ/T/T/T/D). Additional calculations with the completely decontracted def2-TZVP and def2-TZVPP basis sets⁸⁹ were carried out as these basis sets have been employed previously for LPMOs.⁴⁰ A set of calculations were also performed exclusively with standard correlation consistent basis sets but these will not be discussed in detail (see Tables S2 and S3 in the SI).

We selected B3 to carry out calculations on model 1–3 (based on free QM/MM opti-

mizations) with the GGA functionals BLYP^{90,91} and PBE,⁹² the hybrid GGA functionals B3LYP⁹³ and PBE0,^{94–96} the meta-GGA functional TPSS⁶² and the hybrid meta-GGA functional TPSSH⁶² (note that the basis set investigation was carried out using only the B3LYP functional, employing model 1, based on QM/MM optimization with relaxed MM region). In addition, a set of calculations (with all functionals) were done on model 1, based on QM/MM optimizations with unrelaxed MM region. In all calculations on HFCs, a large integration grid for the exchange-correlation functional (Grid7) was employed.

Results and discussion

Calculation of EPR parameters are known to be sensitive to the computational setup, including the underlying structures. The first section therefore discuss the obtained structures, which all are obtained with QM/MM, but employing different QM/MM optimization protocols (as described under Computational Details). In two subsequent subsections, we discuss the basis set, the effect of the chosen DFT functional and the effect of employing models sizes beyond the first coordination sphere of the copper ion. Finally, we discuss our findings in relation to recent studies of the substrate binding process.

Structures

We start with comparing structures obtained with TPSS-D3/def2-SV(P) and the MM region structurally relaxed ("free") and unrelaxed ("fixed"): the optimized structures of the LPMO *Ls*(AA9)A active site with these specifications are shown in Figure 3 both without (a) and with (b) substrate; structures obtained with fixed MM region are shown in green. Selected bond distances are given in Table 1, including results from previous QM/MM optimizations for *Ta*LPMO9A.⁷⁰ It has previously been shown^{27,70} that employing a relaxed MM region has minor effect for intermediates later in the catalytic cycle (after O₂ binds), whereas relaxing the MM region can lead to large differences for both Cu(II) resting state and the Cu(I) state

obtained after initial reduction. The results in Figure 3 and Table 1 confirm this observation for the Cu(II) resting state, where differences are particularly large for substrate-bound structures.

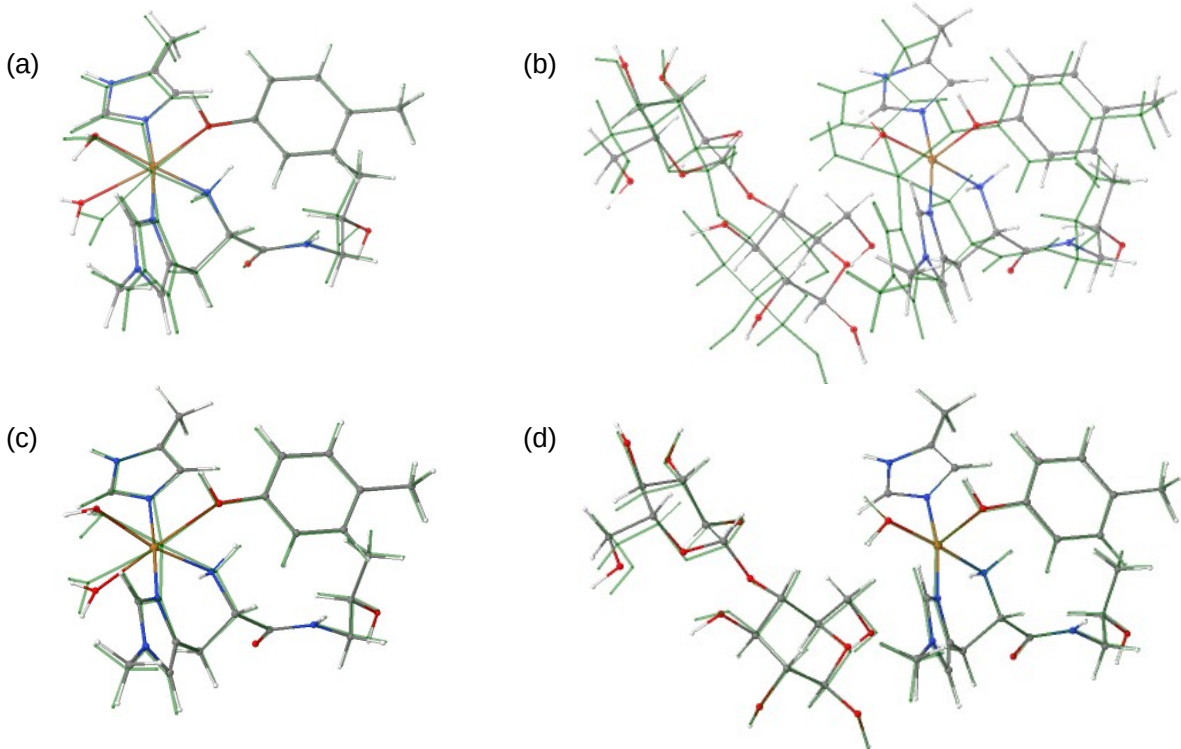


Figure 3: Figures (a) and (b) show overlay of QM/MM TPSS-D3/def2-SV(P) optimizations with the MM region fixed (green) and free (colored) for optimizations without (a) and with (b) substrate. Figures (c) and (d) show overlay of QM/MM optimized structures with free MM region for TPSS-D3/def2-SV(P) (green) and TPSS-D3/def2-TZVPD (colored) for optimizations without (c) and with (d) substrate. Note that all figures display only the QM regions and hence the pocket water is not shown.

A closer look at the obtained distances between the copper center and the first coordination sphere for both optimizations, shows the Cu–N bonds to change minimally, whereas the Cu–O bonds are more sensitive, particularly, bonds along the Jahn-Teller axis, i.e., Cu–O_W^{ax.} and Cu–O_{Tyr}. The Cu–O_{Tyr} bond is generally shorter in the optimizations with parts of the MM region relaxed, but in both cases, Cu–O_{Tyr} decreases upon substrate binding: the bond changes from 2.34 Å to 2.24 Å without substrate, while the corresponding change is 2.42 Å and 2.29 Å for the structure with the entire MM region fixed.

Table 1: Cu–ligand bond lengths (Å) for the active site of LPMO. For brevity, we denote TPSS-D3 and B3LYP-D3 as TPSS and B3LYP, respectively, while we denoted def2-SV(P) and def2-TZVPD as SV(P) and TZVPD.

QM//MM model	Cu–N _{His78} ^ϵ	Cu–N _{His1}	Cu–N _{His1} ^δ	Cu–O _{Tyr}	Cu–O _W ^{ax.}	Cu–O _W ^{eq.}
Optimized without substrate <i>Ls</i> (AA9)A.						
TPSS/SV(P)//Fixed	1.99	2.11	1.97	2.42	2.25	2.16
TPSS/SV(P)//Free	2.03	2.07	2.00	2.34	2.53	2.08
TPSS/TZVPD//Free	2.00	2.09	1.97	2.61	2.34	2.21
Exp. 5ACG ³⁹	2.1	2.2	1.9	2.7	2.8	2.2
Optimized with substrate <i>Ls</i> (AA9)A.						
TPSS/SV(P)//Fixed ²⁷	1.99	2.09	1.95	2.29	-	2.17
TPSS/SV(P)//Free ²⁷	2.06	2.04	2.00	2.24	-	2.04
TPSS/TZVPD//Free	2.04	2.02	1.98	2.26	-	2.03
Exp. 5ACF ³⁹	2.1	1.9	2.2	2.5	-	-
Optimized without substrate (<i>Ta</i> LPMO9A)						
TPSS/SV(P)//Fixed ⁷⁰	2.02	2.07	1.98	2.80	2.28	2.11
TPSS/SV(P)//Free ⁷⁰	2.03	2.03	1.99	2.34	2.83	2.03
TPSS/TZVPD//Free ⁷⁰	2.02	2.02	1.97	2.48	3.00	2.06
B3LYP/TZVPD//Free ⁷⁰	2.04	1.98	2.02	2.47	2.96	2.07
Exp. 2YET ⁷	2.32	2.10	2.43	2.80	2.65	2.23
Exp. 3ZUD ⁷	2.03	2.20	1.91	2.92	2.89	-

When comparing with *Ls*(AA)9 crystal structures with and without substrate (5AFC and 5AFG), it should be noted that although they represent low-dose X-ray structures with minimal photoreduction, partial reduction cannot be excluded. Moreover, the substrate-bound crystal structure (5AFC) binds Cl[−] instead of the equatorial water, meaning that direct comparison is precluded. With these precautions in mind, we still comment on the optimized structures in comparison with the crystallographic results: qualitatively, optimizations with fixed and free MM region both obtain a reduction of the Cu–O_{Tyr} bond distance upon substrate binding (0.1 Å), similar to what is seen from the crystal structures (0.2 Å). Despite this good agreement, larger differences are seen when comparing the absolute distances for

the Cu–O bonds, while Cu–N distance are in quite good correspondance with the crystal structures. The calculated values for Cu–O_{Tyr} are generally shorter than the experimental values, both with and without substrate bound.

Meanwhile, the bond distance for the axial water molecule changes from 2.25 Å (MM fixed) to 2.53 Å (MM relaxed), the latter being closer to the experimentally³⁹ obtained 2.8 Å, but still significantly off. From these results, it seems that the calculations with relaxed MM region obtain structures where both Cu–O_{Tyr} and Cu–O_W^{ax} are elongated which is also seen experimentally, albeit the elongation is less pronounced than seen from the crystal structure. We have previously noted such differences for the weak Cu–O bonds in LPMOs⁷⁰ and a selection of previous QM/MM results are collected in Table 1 (including results from another AA9 LPMO, *Ta*LPMO9A). These results show similar variations among tyrosine and axial water Cu–O bonds, with significant differences both within and between theoretical and crystallographic results. Even larger variations are found, if we also include previous QM-cluster results^{20,97} but these have previously been discussed.⁷⁰ Interestingly, results with relaxed MM regions lead for both *Ls*(AA9)A and *Ta*LPMO9A, to elongation of the Cu–O_W^{ax} bond and shortening of the Cu–O_{Tyr} bond.

In an additional set of calculations, we also optimized structures with a larger basis set, including diffuse functions (def2-TZVPD), still allowing the MM region to structurally relax. The obtained structures are compared to structures overlayed with structures obtained with def2-SV(P) in Figure 3 for substrate-bound (c) and unbound (d) states, respectively. Selected distances are also given in Table 1: the substrate-bound structure is rather unaffected by the use of a larger basis set, while larger changes are seen for the *Ls*(AA9)A structure without substrate: the Cu–O_{Tyr} distance changes from 2.34 Å to 2.61 Å, in better agreement with the experimental value of 2.7 Å. Meanwhile, the distance to Cu–O_W^{ax} becomes shorter (from 2.53 Å to 2.34 Å) which is in worse agreement with the crystal structure (2.8 Å). The distance to the equatorial water molecule, Cu–O_W^{eq} also changes from 2.08 Å to 2.21 Å, where the latter is in better agreement with the crystallographic result (2.2 Å). The differences obtained for

Cu–O bonds between structures optimized with def2-SV(P) and def2-TZVPD (both with the MM region partly relaxed) are not negligible, but the latter is worse for reproducing the EPR hyperfine coupling, as will be discussed further in a section below. In addition to bond-distances, we have also compiled selected bond angles around the Cu atom in Table S1 in the SI. Experimentally, the (selected) angles are all close to 90° , and the calculated values generally comes close, with smaller variations as seen for the bond distances. The largest differences to experiment (8°) is for the structure optimized with MM region fixed (see $N_{\text{His78}}^\epsilon\text{--Cu--O}_{\text{Eq.}}^W$ in Table S1).

In conclusion, the underlying structure (particular the Cu–O distances) can depend significantly on the strategy employed in the optimization, and we will therefore investigate all structures in EPR parameter calculations to quantify how large effect the strategy employed in QM/MM optimizations have on the obtained parameters. However, we first investigate the influence of the employed basis set in next section.

Basis set study of hyperfine coupling parameters

The basis sets regularly employed in quantum chemical calculations are not optimized to be accurate in the atomic core region. Hence, the part of the EPR spin-Hamiltonian, depending on the core spin-density (i.e. the HFCs) can become erratic, if not specially designed core-property basis sets are employed.^{53,75–80,98–107} An alternative is to decontract a regular basis set to make it more flexible in the core region. Here we investigate both strategies, employing the aug-cc-pVTZ-J basis sets^{53,75–80} as well as the decontracted def2-TZVP and def2-TZVPP basis sets⁸⁹ (which were employed in Ref. 40). Since both strategies results in rather large basis sets, we additionally investigate a locally-dense strategy, where aug-cc-pVTZ-J is employed locally on the nuclei of interest, while smaller basis sets are employed for the remaining nuclei. We and others have previously shown this strategy to work well^{81–85} also for systems containing transition metals.⁸⁴ However, to the best of our knowledge, no systematic studies have yet been performed to test if this strategy works well for LPMOs

(or indeed any other copper proteins).

Table 2: Effect of employed basis on the HFC (in MHz) of Cu with B3LYP (LPMO model 1 in Figure 2, optimized without substrate and TPSS-D3/def2-SV(P) with the MM region relaxed). CGTOs is the number of contracted Gaussian functions in the basis set.

Basis	# CGTOs	A^{FC}	$A_{\text{iso}}^{\text{SO}}$	A_{11}	A_{22}	A_{33}	A_{iso}
aT/aT/aT/aT/aT	1910	198.2	138.3	-89.6	509.2	589.7	336.5
B1: aTJ/T/T/T/D	1016	-252.6	135.7	47.4	126.7	-524.8	-116.9
B2: aTJ/aTJ/T/T/D	1112	-251.9	135.8	47.9	127.7	-524.0	-116.1
B3: aTJ/aTJ/aTJ/T/D	1240	-252.2	135.8	47.7	127.4	-524.3	-116.4
B4: aTJ/aTJ/aTJ/aTJ/D	1416	-257.1	135.7	42.7	122.4	-529.3	-121.4
B5: aTJ/aTJ/aTJ/aTJ/T	1677	-252.3	135.8	47.8	127.1	-524.5	-116.5
B6: aTJ/aTJ/aTJ/aTJ/aTJ	1851	-252.3	135.8	47.8	127.1	-524.5	-116.5
TZVP-uncontracted	1474	-245.4	133.3	51.8	124.0	-512.1	-112.1
TZVPP-uncontracted	1725	-245.2	132.4	53.4	127.5	-512.2	-112.8
Exp.	-	-	-	58	78	-458	-107

Table 3: Effect of employed basis on the isotropic part of HFCs (in MHz) for the coordinating N atoms with B3LYP (LPMO model 1 in Figure 2, optimized without substrate and TPSS-D3/def2-SV(P) and MM region relaxed). CGTOs is the number of contracted Gaussian functions in the basis set.

Basis	# CGTOs	$A_{\text{iso}} (N_{\text{His1}}^{\delta})$	$A_{\text{iso}} (N_{\text{His1}})$	$A_{\text{iso}} (N_{\text{His78}}^{\epsilon})$
aT/aT/aT/aT/aT	1910	36.1	39.1	36.3
B1: aTJ/T/T/T/D	1016	35.8	39.2	36.1
B2: aTJ/aTJ/T/T/D	1112	38.6	42.8	38.9
B3: aTJ/aTJ/aTJ/T/D	1240	38.6	42.8	38.9
B4: aTJ/aTJ/aTJ/aTJ/D	1416	38.6	42.8	38.9
B5: aTJ/aTJ/aTJ/aTJ/T	1677	38.6	42.8	38.9
B6: aTJ/aTJ/aTJ/aTJ/aTJ	1851	38.6	42.8	38.9
TZVP-uncontracted	1474	37.8	41.9	38.1
TZVPP-uncontracted	1725	37.5	41.6	37.8

We chose to carry out the basis set study on the smallest model without substrate, i.e., model 1 in Figure 2; optimized with TPSS-D3/def2-SV(P) and the MM region relaxed. The

effect of enlarging the model on the calculated HFCs is investigated in next subsection. We next constructed several locally-dense basis sets with aug-cc-pVTZ-J on an increasing number of atoms and smaller, standard Dunning basis sets on the other atoms (B1–B6, see Computational Details).

The results from the basis set investigation are compiled in Table 2 for the copper atom and Table 3 for the nitrogen atoms in the first coordination sphere. We consider the results with the aT/aT/aT/aT/aT combination of basis sets as best values obtained with standard basis sets and results with B6 are the best values obtained.

Starting with the copper atom, Table 2 shows the expected large effect of using core-property basis sets on the isotropic Fermi contact (FC) and the anisotropic spin-dipolar terms. The FC term changes by as much as 450 MHz and therefore also changes sign. The changes in some of the components of the hyperfine tensor, e.g. A_{33} , are with about 1100 MHz even larger. Interestingly, the second-order spin-orbit contribution almost does not change. With the standard aug-cc-pVTZ basis set on all atoms it amounts to 138 MHz, with the core-property basis set aug-cc-pVTZ-J on all atoms (B6) 136 MHz, and with the decontracted standard def2-TZVP and def2-TZVPP basis sets around 133 MHz. Slightly larger changes are observed on going to the smaller standard basis sets like cc-pVTZ and cc-pVDZ as shown in Table S2 in the SI, but reasonable results (between 141 and 138 MHz) are still obtained. This basis set insensitivity of the spin-orbit contribution implies that the change with respect the employed basis set for the total isotropic hyperfine coupling originates almost exclusively from the Fermi contact term. It is worthwhile to mention, that (as expected) spin-orbit effects are quite large for the HFCs of Cu in LPMO: as one can see from Table 2, the second-order spin-orbit contribution is approximately 50% of the Fermi contact contribution but with opposite sign and thus essential to include in the calculations.

While it is clear that specialized basis sets must be employed on the Cu atom, employing aug-cc-pVTZ-J only on Cu gives values within 1 MHz of the results where all atoms have aug-cc-pVTZ-J basis sets. Additionally employing aug-cc-pVTZ-J on the first coordination

sphere and the imidazole rings also has minimal effect. Hence, our study shows that we can safely employ a local-dense strategy, thereby reducing the number of contracted functions considerably. In the following we will therefore continue with basis set B3. The result with this basis set, -116 MHz for A_{iso} , differs by about 4 MHz from the results obtained with the decontracted standard triple zeta basis sets, def2-TZVP and def2-TZVPP, which were employed in Ref. 40, although this covers over differences of 7 MHz in the FC term and 3 MHz in the spin-orbit contribution with opposite signs.

Turning to nitrogen super HFCs, we see from Table 3 that as soon as one uses a core-property basis set on the nitrogen atoms of interest (B2), the choice of basis set on the other atoms does not make a difference anymore. The totally decontracted standard polarized triple zeta basis sets, def2-TZVP and def2-TZVPP, leads to values for the super HFCs, which are 1 MHz smaller still.

We have also investigated various locally-dense combinations of the regular Dunning basis sets (shown in the SI, Tables cf. Table S2 and S3), but the results where (as expected) erratic for the copper HFCs leading to errors of over 300 MHz compared to results with the aug-cc-pVTZ-J basis set on Cu, even when using the aug-cc-pVTZ basis set on all atoms (aT/aT/aT/aT/aT in Table 2). These results will therefore not be discussed in detail, although we note that reasonable results were obtained for HFCs of the nitrogen atoms with the regular Dunning basis sets.

The effect of functional and underlying structure

From previous section, we have selected the basis set denoted "B3", and we now proceed to consider the effect of the employed DFT functional as well as the underlying structure on the calculated HFCs. The latter is considered in two aspect: first, we consider an indirect structural effect by employing QM/MM optimized structures with fixed MM region and compare these results to structures with (parts of) the MM region free. For the latter structures we further extend the size of the systems employed for the calculations of HFCs

as shown in Figure 2. The different structures are investigated with a range of DFT functionals to see how well the calculated HFCs (for a given structure and functional) reproduce the experimentally observed trend upon substrate binding. We also comment on how well the (absolute) experimental HFCs are reproduced by the various computational setups. In relation to comparison with experiment, it should be noted that we here investigate all (principal) components of the copper HFCs, although the fitting used to extract the HFCs from experimental spectra usually only allows accurate determination of $|A_z|$ (here denoted A_{33}). Regarding the nitrogen HFCs, only the isotropic values could be resolved for the investigated *Ls*(AA9)A enzyme, and no assignment to individual nitrogen atoms was achieved.³⁹

Table 4: Cu HFCs (in MHz) calculated with different functionals and basis set B3 (see Computational Details). All calculations were done on model 1, obtained with an underlying structure from QM/MM TPSS-D3/def2-SV(P) with fixed MM region.

With substrate	A^{FC}	$A_{\text{iso}}^{\text{SO}}$	A_{11}	A_{22}	A_{33}	A_{iso}
PBE0	-198.4	150.0	84.6	221.7	-451.4	-48.4
PBE	-89.5	97.2	118.3	225.9	-321.3	7.7
B3LYP	-151.6	136.7	119.8	247.1	-411.4	-14.9
BLYP	-66.4	95.0	138.1	248.3	-300.5	28.6
TPSSh	-140.0	106.5	104.4	226.3	-431.1	-33.5
TPSS	-95.1	90.1	114.6	232.9	-362.7	-5.0
Exp.	-	-	20	38	-515	-152
Without substrate	A^{FC}	$A_{\text{iso}}^{\text{SO}}$	A_{11}	A_{22}	A_{33}	A_{iso}
PBE0	-198.1	153.4	33.1	275.1	-442.4	-44.7
PBE	-96.6	98.7	60.3	269.0	-323.3	2.0
B3LYP	-153.0	139.9	65.4	300.1	-404.6	-13.0
BLYP	-72.2	96.6	80.7	293.6	-301.1	24.4
TPSSh	-142.0	108.7	47.9	279.2	-427.2	-33.4
TPSS	-99.4	91.5	57.7	280.9	-362.2	-7.9
Exp.	-	-	58	78	-458	-107

Hyperfine coupling constants from structures with fixed MM region

We start by investigating the obtained differences in copper HFCs for substrate-free and substrate-bound states, when employing a structurally fixed MM region (and model 1 in Figure 2). The HFCs for copper with this setup are shown in Figure 4 and the underlying values are provided in Table 4. The calculated copper HFCs are significantly off the ex-

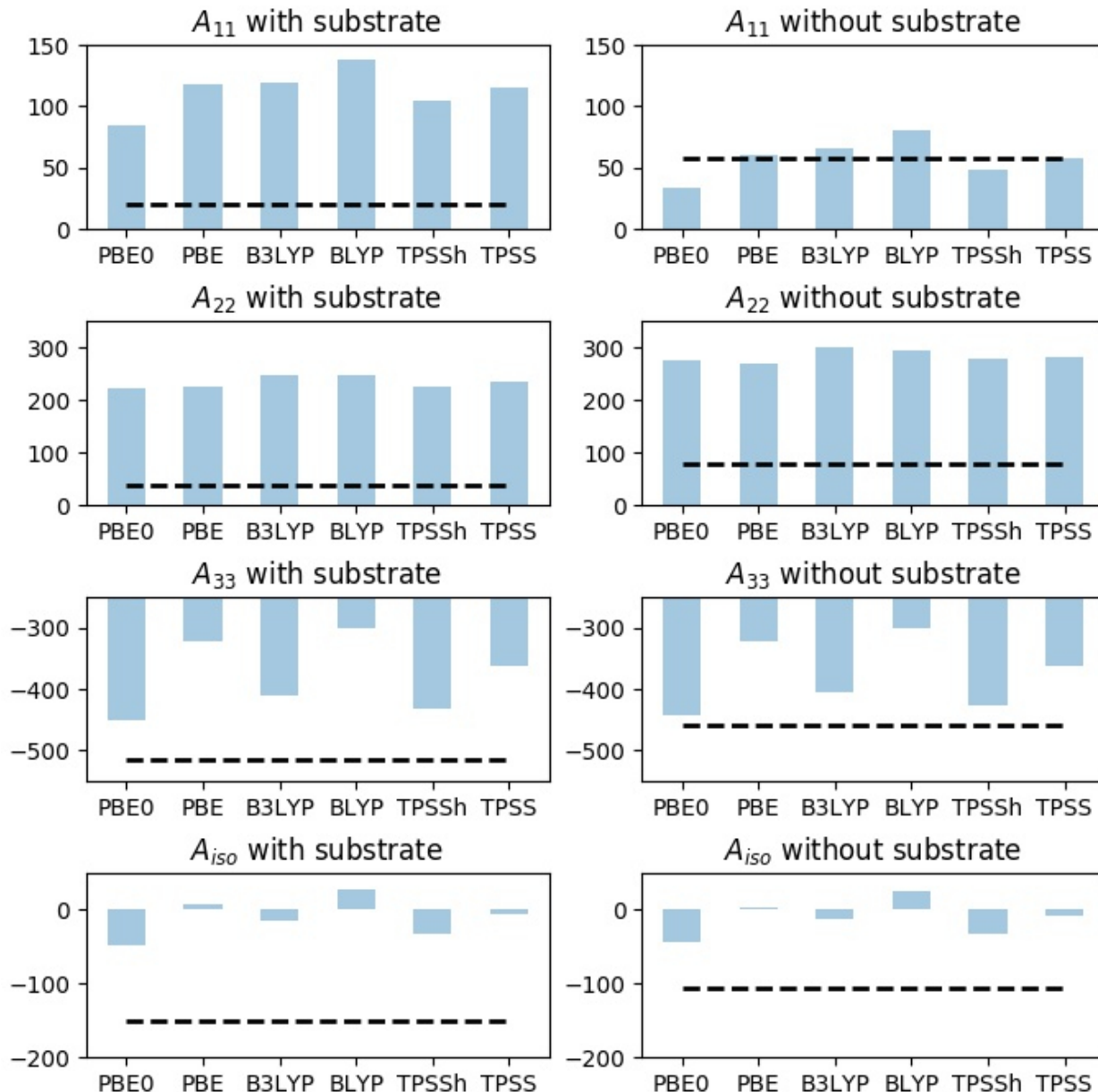


Figure 4: Calculated HFCs (in MHz) for copper over six different functionals, all calculated on model 1 with underlying structure QM/MM structures optimized with TPSS-D3/def2-SV(P) and the MM region fixed. Black dashed lines are experimental values.

perimental values for all three components of the HFC tensor for structures with substrate present (see Figure 4); the A_{11} and A_{22} components are severely underestimated, while the A_{33} component is severely overestimated (in absolute values). While the results look better for A_{11} for the substrate-free structure, both A_{22} and A_{33} still show large deviations (with most functionals) from the experimental values.

From Table 4 (and Figure 4) we further see that the change in HFCs observed when the substrate binds is not always reproduced. For instance, the change of A_{33} values is estimated considerably too small and sometimes in the wrong direction: we obtained changes between 7 and -2 MHz, compared to the experimental value of 57 MHz. Regarding the other two components of the HFC tensor, the A_{11} values all decrease (between 51–57 MHz, cf. Table 5), whereas this is opposite experimentally (increase of 38 MHz). The qualitative changes for A_{22} are reasonably well reproduced, with an increase of 48–54 MHz, compared to the experimental 40 MHz. However, it is clear from Figure 4 that this is due to error compensation due to the above-mentioned overestimation of A_{22} in both substrate-bound and substrate-free structures.

In next section, we discuss QM/MM structures with the MM region relaxed, but a preliminary assessment of the importance of the underlying structure can be done by comparing the B3LYP results in Table 4 with the B3 results from Table 2 (which also were done with model 1, but based on a structure optimized with the MM part relaxed). From this, we see that the underlying structure to be pertinent and the structures based on QM/MM optimization with relaxed MM region seem to perform significantly better: in particular, an approximately axial A-tensor is obtained, while all functionals in Table 4 lead to an A-tensor with pronounced rhombicity ($A_{11} \neq A_{22} \neq A_{33}$), which does not commensurate with experiment.³⁹ We can also make a preliminary estimate of the importance of the chosen functional: as expected, the functionals in Table 4 yield HFCs that are significantly different between different choices, but a more through discussion is postponed to next section, since none of the functionals obtain qualitatively correct results based on a fixed MM region.

Finally, we also comment on the nitrogen (super) HFCs. Here only isotropic values have been obtained for the LPMO targeted in this study.³⁹ The values obtained from the experimental spectrum with the substrate bound were 36, 30 and 19 MHz. Our calculated values (Table S4) are in the range 30–48 MHz and thus in reasonable agreement with these values. Similarly, without substrate we obtain quite similar values (35, 41 and 36 MHz). In this case, it was only possible to experimentally resolve two of the nitrogen HFCs (37 and 34 MHz). We again postpone the discussion to the use of more accurate structures below, but we note that nitrogen HFCs are much less sensitive to the underlying structure than copper HFCs.

Hyperfine coupling constants from structures with free MM region

Results based on structures obtained from QM/MM methods, where the MM region is allowed to structurally relax are shown in Figure 5 and concrete values are given in Table 5. As implied in last section, we already for (the smallest) model 1 obtain values that are overall in better agreement with experiment, compared to results with the MM region fixed (this holds for all functionals). To ensure that the better correspondence with experiment is not a fortuitous result due to the chosen system size, we included first the "pocket" water molecule³⁹ connecting the terminal NH_2 group of His1 with the substrate through hydrogen bonding (model 2 in Figure 2). Next, we included parts of the substrate (model 3) to investigate if the substrate had a direct effect on the electronic structure, and hence on the HFCs. The HFCs calculated with these three model sizes are shown in different colored bars in Figure 5 (and are also provided in Table 5). Generally, the largest effect is seen when including the water molecule (i.e. between models 1 and 2), most pronounced for A_{22} . Still, for all model sizes the results are in general in better agreement with experimental values, compared to results for the fixed structure. Thus, the method employed in optimization of the underlying structure is among the most critical factors for accurate HFCs; the same holds true for the employed DFT functional, which now will investigate in more detail.

Table 5: Calculated HFCs (in MHz) for copper with basis set B3, employing six different functionals. All calculations are on QM/MM structures, optimized with TPSS-D3/def2-SV(P) where the MM region is allowed to relax. The calculations on the substrate-bound state were done with three models of different sizes (cf. Figure 2).

With substrate	A^{FC}	$A_{\text{iso}}^{\text{SO}}$	A_{11}	A_{22}	A_{33}	A_{iso}
<u>Model 1</u>						
PBE0	-323.7	142.5	6.2	42.9	-592.7	-181.2
PBE	-213.3	91.9	21.7	75.2	-461.1	-121.4
B3LYP	-282.4	129.7	30.9	68.0	-557.1	-152.7
BLYP	-192.6	90.0	39.0	96.2	-443.0	-102.6
TPSSh	-269.2	101.8	5.5	52.8	-570.4	-167.4
TPSS	-222.2	86.0	22.0	72.6	-503.3	-136.2
<u>Model 2</u>						
PBE0	-333.1	140.8	-0.4	25.4	-602.0	-192.3
PBE	-223.5	91.0	19.6	57.2	-474.3	-132.5
B3LYP	-293.0	128.0	23.6	48.6	-567.3	-165.0
BLYP	-203.6	89.1	36.4	77.6	-457.5	-114.5
TPSSh	-279.1	100.6	9.9	34.0	-579.4	-178.5
TPSS	-232.9	85.1	19.2	53.2	-515.8	-147.8
<u>Model 3</u>						
PBE0	-335.8	138.1	-8.0	18.4	-603.7	-197.8
PBE	-227.0	89.2	21.8	45.5	-480.7	-137.8
B3LYP	-296.0	125.2	15.8	40.8	-568.7	-170.7
BLYP	-207.4	87.3	36.7	67.2	-464.0	-120.1
TPSSh	-280.8	98.6	4.9	26.7	-578.1	-182.2
TPSS	-235.2	83.4	20.0	42.5	-517.9	-151.8
Exp.	-	-	20	38	-515	-152
Without substrate	A^{FC}	$A_{\text{iso}}^{\text{SO}}$	A_{11}	A_{22}	A_{33}	A_{iso}
<u>Model 2'</u>						
PBE0	-305.7	147.4	13.3	82.1	-570.3	-158.3
PBE	-204.7	97.3	49.7	95.2	-467.1	-107.4
B3LYP	-264.3	134.3	40.6	105.9	-536.4	-130.0
BLYP	-183.3	95.6	69.0	119.1	-451.1	-87.7
TPSSh	-252.7	105.1	27.7	85.2	-555.7	-147.6
TPSS	-210.9	89.7	46.2	94.4	-504.2	-121.2
Exp.	-	-	58	78	-458	-107

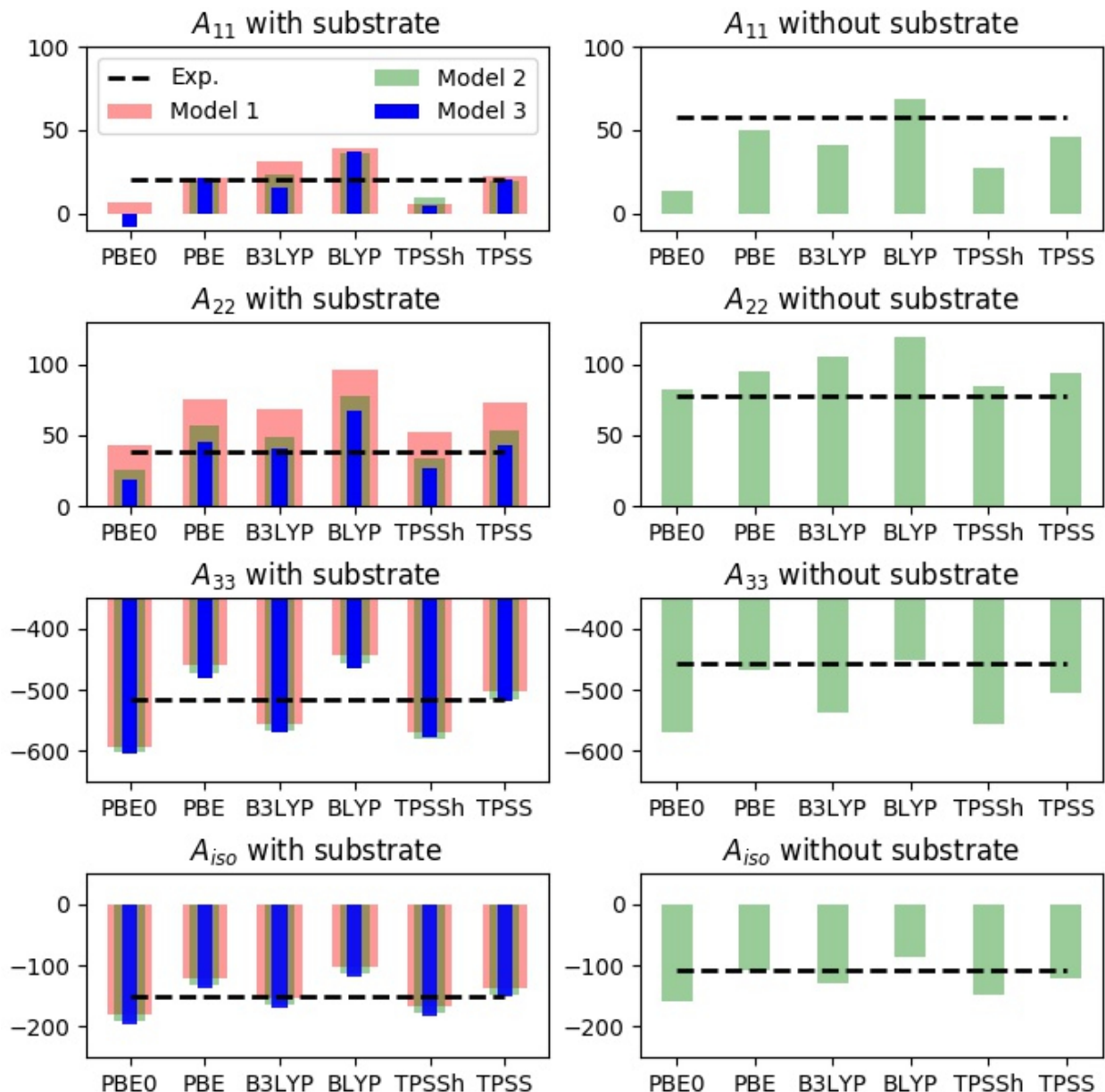


Figure 5: Calculated HFCs (in MHz) for copper over six different functionals, all calculated on QM/MM structures optimized with TPSS-D3/def2-SV(P) and the MM region allowed to relax. The calculations on the substrate-bound state were done with three models of different sizes (cf. Figure 2).

We focus here on the largest models i.e. model 3 for the substrate-bound structure and model 2 for the structure without substrate, cf. Figure 2. For these models all functionals reproduce the changes in the A-tensor upon substrate binding observed experimentally, at least qualitatively. Thus, the absolute values of the A_{33} component increase with 57 MHz

experimentally, while we obtain calculated values between 14 and 32 MHz. Meanwhile, for A_{11} the experimental value decreases 38 MHz upon substrate binding, while our theoretical values are between 21 and 33 MHz, depending on the functional (which is in reasonable correspondence with the experiment). Similarly, for A_{22} the calculated values decrease with 50–64 MHz, compared to the experimentally measured decrease of 40 MHz.

While the results generally reproduce the experimentally observed change in HFCs for the copper atom, we should still comment on the large differences in the absolute values between the functionals. For both substrate-bound and unbound states, individual differences between the functionals far surpass differences induced by the chosen model size. Starting with the substrate-bound structure, the absolute value of A_{33} is the largest of the three HFC components and also where we obtained the largest (absolute) differences between the different functionals, ranging from underestimation of 89 MHz (PBE0) to overestimation of 32 MHz (BLYP). For A_{11} all functionals except PBE0 obtain results in reasonable agreement with the 20 MHz, obtained experimentally. A general trend is that the inclusion of exact exchange into the functionals seem to lower the obtained value: for PBE0 this lowering leads to a negative sign, and PBE0 is also in largest disagreement with experiment in absolute numbers (28 MHz). The results for A_{22} are also overall reasonable; the largest difference is here obtained for BLYP, overestimating the experimental results by 29 MHz. Again, we note that inclusion of exact exchange always lead to increase of A_{22} .

Moving to the unbound state, the different functionals show somewhat larger scatter, suggesting this state is in fact more difficult than the bound state. The A_{33} value is the largest and also shows the largest spread in values: thus BLYP overestimates the value with 7 MHz, while PBE0 underestimates with 112 MHz. Including exact exchange generally leads to an increase in the absolute values. The A_{11} component spans values from 13 MHz with PBE0 (underestimation of 44 MHz) to 69 MHz with BLYP (overestimation of 11 MHz). The values for A_{22} are generally below the experimental value, ranging from a value of 119 MHz (41 MHz from the experiment) with BLYP to 82 MHz with PBE0, which is only 4 MHz

from experiment. Functionals including exact exchange always give larger values, compared to the same functional without exact exchange.

As previously noted, the nitrogen HFCs are much less dependent on the computational setup. Thus, values obtained with underlying QM/MM structures with the MM region relaxed (Table S5), are rather similar to the HFCs obtained from underlying QM/MM structures obtained with the MM region fixed. Moreover, the values in Tables S4 and S5 show that nitrogen HFCs are fairly independent on the employed functional.

The nitrogen HFCs for the substrate-bound complex and the active site without substrate are similar in absolute size to the values obtained in Ref. 39. However, without an experimental assignment to the individual atoms, it is difficult to make more precise comparisons. Intriguingly, our values in Table S5 are in quite good correspondence with the values obtained with DFT (PBE0) for a substrate-bound AA10 LPMO (*SmAA10A*) in Ref. 40: here they obtained 39 MHz for A_{iso} of N_{His1} and 32 MHz for A_{iso} of both N_{His1}^{δ} and $N_{\text{His78}}^{\epsilon}$ (using the nomenclature for *Ls(AA9)A*). Notably, these values were used in fitting of experimental spectra, yielding simulated spectra that closely resembled the experimental ones. Hence, it would be interesting to employ the values obtained here in a similar fashion.

We have also calculated copper and nitrogen HFCs on model 3, employing an underlying structure obtained with def2-TZVPD (see Figure 3). We will not discuss the results in the same detail, and we have compiled the resulting HFCs in the SI (Tables S6 and S7). We note that the structure of the substrate-bound state is close to unchanged and as expected, quite small changes in the obtained HFCs are therefore seen. However, the structure of the unbound state changes (as described in a previous section), mainly around the Cu–O bonds from the water molecule and tyrosine. As one might expect, this also affects the obtained HFCs for copper (again, the changes in nitrogen HFCs are much smaller). The HFCs are still qualitatively correct: for instance the A_{33} values generally increase (between 123 and 136 MHz), but are often in less good agreement with the experimental values, compared to calculations carried out on structures optimized with def2-SV(P). Particularly the A_{22} values

are too large making the A-tensor more rhombic than axial; while it may seem that def2-SV(P) is the better choice, we should emphasize that to obtain results directly comparable with experiment, inclusion of system dynamics is pertinent, particular as the Cu–O bonds are rather weak and the calculated copper HFCs are highly dependent on these bonds.

In comparison to AA10 LPMOs, the decreasing A_{11} and A_{22} values, accompanied by an increasing A_{33} -value upon substrate binding are also seen for the *SmAA10A* and *B/LPMO10A*^{40,43} LPMOs; DFT was able to qualitatively reproduce the observed changes, although large differences were seen with respect to experiment. Our results here show that the findings from AA10 LPMOs can be transferred to *Ls(AA9)A*, and DFT also reproduces the observed trend upon substrate binding (although it is highly dependent on the used starting structure). In Ref.,⁴³ the different contributions to the HFCs were analyzed and it was found that the main change was due to the FC term. Our results also agree that the changes in the FC term are the largest upon substrate binding (22–26 MHz), compared to the contributions from spin-orbit coupling (7–9 MHz), as seen from Table 5. We also find the FC term to be more negative after substrate binding (the SO contribution is positive and increases), as discussed in Ref. 43; thus the changes of the HFCs seem to operate through the same mechanism in *Ls(AA)9* and *B/LPMO10A*.

Conclusion and outlook

We have calculated copper and nitrogen HFCs for the active site of the LPMO *Ls(AA9)A*, both in a substrate-unbound and a substrate bound state. The HFCs change upon substrate binding, and we have investigated whether DFT can reproduce the experimental trend. We find that this is possible, but the quality of the result is highly dependent on the computational setup. As expected, it is important to employ core-property basis sets in these calculations, otherwise the values for the Fermi contact and spin-dipolar contributions will be far off. However, these basis sets are only necessary for the atoms, which couplings are

to be calculated, i.e. the use of locally-dense basis sets allows to reduce the size of the basis sets significantly. Perhaps more importantly, it is crucial to allow the MM region to relax (we use 6 Å from the QM region): employing a structurally relaxed MM region gives copper A-tensors that are approximately axial (for all functionals employed), while optimizations with the MM region fixed led to A-tensors where the principal components were very different (rhombic). In the latter case, some functionals also fail to reproduce the observed trend upon substrate binding. Nitrogen HFCs are much less sensitive to computational setup, and are generally obtained in reasonable correspondence to experimental values.

All employed functionals obtained qualitatively correct changes of the HFCs upon substrate binding (if structures with partly relaxed MM region are used). However, there are considerable differences between the individual functionals. Our study we find that both PBE and TPSS perform well for the non-hybrid functionals while B3LYP and TPSSh perform well for the hybrid functional. However, before addressing which of these functionals that perform best, it would be desirable to include system dynamics, since large structural differences obtained for the weak Cu–O bonds, which again have large influence on the obtained HFCs. Thus, employing different starting structures from molecular dynamics may change the ordering found here. Another way of probing the functional performance would be against high-accurate data (e.g. two or four component relativistic methods), which would also be desirable. Further measures to improve the accuracy (within a one-component DFT framework) would be to employ a scalar-relativistic Hamiltonian, e.g., the zeroth order regular approximation (ZORA). Second, our present calculations have not considered the direct electrostatic effect of the protein. Results from blue copper proteins⁴⁶ indicate that ZORA as well as electrostatic effects are non-negligible (both between 10–30 MHz), but generally below the differences we find between the different DFT functionals.

Acknowledgement

EDH acknowledges financial support from the European Commission (MetEmbed project 745967) and the Villum Foundation (Young Investigator Program, Grant No. 29412). LLL acknowledges financial support by the Novo Nordisk Foundation HOPE project (NNF17SA0027704).

Supporting Information Available

Selected bond angles for QM/MM optimized structures. Results for the hyperfine couplings with the various (regular) mixed Dunning basis sets

References

- (1) Harris, P. V.; Welner, D.; McFarland, K. C.; Re, E.; Poulsen, J.-C. N.; Brown, K.; Salbo, R.; Ding, E., H. Vlasenko; Merino, S.; Xu, F.; Cherry, J.; Larsen, S.; Lo Leggio, L. Stimulation of lignocellulosic biomass hydrolysis by proteins of glycoside hydrolase Family 61: Structure and Function of a Large, Enigmatic Family. *Biochemistry* **2010**, *49*, 3305–3316.
- (2) Vaaje-Kolstad, G.; Westereng, B.; Horn, S. J.; Liu, Z.; Zhai, M., H. Sørlie; Eijsink, V. G. H. An oxidative enzyme boosting the enzymatic conversion of recalcitrant polysaccharides. *Science* **2010**, *330*, 219–222.
- (3) Klemm, D.; Heublein, B.; Fink, H.-P.; Bohn, A. Cellulose: Fascinating biopolymer and sustainable raw material. *Angew. Chem. Int. Ed.* **2005**, *44*, 3358–3393.
- (4) Lombard, V.; Ramulu, H. G.; Drula, E.; Coutinho, P. M.; Henrissat, B. The carbohydrate-active enzymes database (CAZy) in 2013. *Nucleic Acids Research* **2013**, *42*, D490–D495.
- (5) Eibinger, M.; Ganner, T.; Bubner, P.; Rosker, S.; Kracher, D.; Haltrich, D.; Ludwig, R.; Plank, H.; Nidetzky, B. Cellulose surface degradation by a Lytic polysaccharide monooxygenase and its Effect on cellulase hydrolytic efficiency. *J. Biol. Chem.* **2014**, *289*, 35929–35938.
- (6) Frandsen, K. E. H.; Lo Leggio, L. Lytic polysaccharide monooxygenases: a crystallographer’s view on a new class of biomass-degrading enzymes. *IUCrJ* **2016**, *3*, 448–467.

- (7) Quinlan, R. J. et al. Insights into the oxidative degradation of cellulose by a copper metalloenzyme that exploits biomass components. *Proc. Nat. Sci. USA* **2011**, *108*, 15079–15084.
- (8) Hemsworth, G. R.; Henrissat, B.; Davies, G. J.; Walton, P. H. Discovery and characterization of a new family of lytic polysaccharide monooxygenases. *Nat. Chem. Biol.* **2014**, *10*, 122–126.
- (9) Vu, V. V.; Beeson, W. T.; Span, E. A.; Farquhar, E. R.; Marletta, M. A. A family of starch-active polysaccharide monooxygenases. *Proc. Natl. Acad. Sci. USA* **2014**, *111*, 13822–13827.
- (10) Lo Leggio, L. et al. Structure and boosting activity of a starch-degrading lytic polysaccharide monooxygenase. *Nat. Commun.* **2015**, *6*, 5961.
- (11) Couturier, M. et al. Lytic xylan oxidases from wood-decay fungi unlock biomass degradation. *Nat. Chem. Biol.* **2018**, *14*, 306–310.
- (12) Sabbadin, F. et al. An ancient family of lytic polysaccharide monooxygenases with roles in arthropod development and biomass digestion. *Nat. Commun* **2018**, *756*.
- (13) Filiatrault-Chastel, C.; Navarro, D.; Haon, M.; Grisel, S.; Herpoël-Gimbert, I.; Chevret, D.; Fanuel, M.; Henrissat, B.; Heiss-Blanquet, S.; Margeot, A.; Berrin, J.-G. AA16, a new lytic polysaccharide monooxygenase family identified in fungal secretomes. *Biotechnol. Biofuels* **2019**, *12*, 55.
- (14) Isaksen, T.; Westereng, B.; Aachmann, F. L.; Agger, J. W.; Kracher, D.; Kittl, R.; Ludwig, R.; Haltrich, D.; Eijsink, V. G. H.; Horn, S. J. A C4-oxidizing lytic polysaccharide monooxygenase cleaving both cellulose and cello-oligosaccharides. *J. Biol. Chem.* **2014**, *289*, 2632.

- (15) Bennati-Granier, C.; Garajova, S.; Champion, C.; Grisel, S.; Haon, M.; Zhou, S.; Fanuel, M.; Ropartz, D.; Rogniaux, H.; Gimbert, I.; Record, E.; Berrin, J.-G. Substrate specificity and regioselectivity of fungal AA9 lytic polysaccharide monooxygenases secreted by *Podospora anserina*. *Biotechnol. Biofuels* **2015**, *8*, 90.
- (16) Agger, J. W.; Isaksen, T.; Várnai, A.; Vidal-Melgosa, S.; Willats, W. G. T.; Ludwig, R.; Horn, S. J.; Eijsink, V. G. H.; Westereng, B. Discovery of LPMO activity on hemicelluloses shows the importance of oxidative processes in plant cell wall degradation. *Proc. Natl. Sci. USA* **2014**, *111*, 6287–6292.
- (17) Frommhagen, M.; Sforza, S.; Westphal, A. H.; Visser, J.; Hinz, S.; Koetsier, M. J.; van Berkel, W. J. H.; Gruppen, H.; Kabel, M. A. Discovery of the combined oxidative cleavage of plant xylan and cellulose by a new fungal polysaccharide monooxygenase. *Biotechnol. Biofuels* **2015**, *8*, 101.
- (18) Hemsworth, G. R.; Davies, G. J.; Walton, P. H. Recent insights into copper-containing lytic polysaccharide mono-oxygenases. *Curr. Opin. Struct. Biol.* **2013**, *23*, 660–668.
- (19) Span, E. A.; Marletta, M. A. The framework of polysaccharide monooxygenase structure and chemistry. *Curr. Opin. Struct. Biol.* **2015**, *35*, 93–99.
- (20) Kim, S.; Ståhlberg, J.; Sandgren, M.; Patond, R. S.; Beckham, G. T. Quantum mechanical calculations suggest that lytic polysaccharide monooxygenases use a copper-oxyl, oxygen-rebound mechanism. *Proc. Natl. Sci. USA* **2014**, *111*, 149–154.
- (21) Beeson, W. T.; Vu, V. V.; Span, E. A.; Phillips, C. M.; Marletta, M. A. Cellulose Degradation by Polysaccharide Monooxygenases. *Annu. Rev. Biochem.* **2015**, *84*, 923–946.
- (22) Walton, P. H.; Davies, G. J. On the catalytic mechanisms of lytic polysaccharide monooxygenases. *Curr. Opin. Chem. Biol.* **2016**, *31*, 195–207.

- (23) Hedegård, E. D.; Ryde, U. Targeting the reactive intermediate in polysaccharide monooxygenases. *J. Biol. Inorg. Chem.* **2017**, *22*, 1029–1037.
- (24) Vaaje-Kolstad, G.; Forsberg, Z.; Loose, J. S. M.; Bissaro, B.; Eijsink, V. G. H. Structural diversity of lytic polysaccharide monooxygenases. *Curr. Opin. Struct. Biol.* **2017**, *44*, 67–76.
- (25) Bertini, L.; Lambrughi, M.; Fantucci, P.; De Gioia, L.; Borsari, M.; Sola, M.; Bortolotti, C. A.; Bruschi, M. Catalytic mechanism of fungal lytic polysaccharide monooxygenases investigated by first-principles calculations. *Inorg. Chem.* **2017**, *57*, 86–97.
- (26) Wang, B.; Johnston, E. M.; Li, P.; Shaik, S.; Davies, G. J.; Walton, P. H.; Rovira, C. QM/MM studies into the H₂O₂-dependent activity of lytic polysaccharide monooxygenases: Evidence for the formation of a caged hydroxyl radical intermediate. *ACS Catalysis* **2018**, *8*, 1346–1351.
- (27) Hedegård, E. D.; Ryde, U. Molecular mechanism of lytic polysaccharide monooxygenases. *Chem. Sci.* **2018**, *9*, 3866–3880.
- (28) Bissaro, B.; Streit, B.; Isaksen, I.; Vincent G. H. Eijsink, V. G. H.; Beckham, G. T.; Røhr, Å. K. Molecular mechanism of the chitinolytic peroxygenase reaction. *Proc. Natl. Sci. U.S.A.* **2020**, *117*, 1504–1513.
- (29) Bissaro, B.; Røhr, Å. K.; Müller, G.; Chylenski, P.; Skaugen, M.; Horn, S. J.; Vaaje-kolstad, G.; Eijsink, V. G. H. Oxidative cleavage of polysaccharides by monocopper enzymes depends on H₂O₂. *Nat. Chem. Biol.* **2017**,
- (30) Hangasky, J. A.; Iavarone, A. T.; Marletta, M. A. Reactivity of O₂ versus H₂O₂ with polysaccharide monooxygenases. *Proc. Natl. Acad. Sci. USA* **2018**,

- (31) Vaaje-kolstad, G.; Houston, D. R.; Riemen, A. H. K.; Eijsink, V. G. H.; van Aalten, D. M. F. crystal structure and binding properties of the serratia marcescens chitin-binding protein CBP21. *J. Biol. Chem.* **2005**, *280*, 11313–11319.
- (32) Vu, V. V.; Beeson, W. T.; Phillips, C. M.; Cate, J. H. D.; Marletta, M. A. Determinants of regioselective hydroxylation in the fungal polysaccharide monooxygenases. *J. Am. Chem. Soc.* **2014**, *136*, 562–565.
- (33) Aachmann, F. L.; Sørlie, M.; Skjåk-Bræk, G.; Eijsink, V. G. H.; ; Vaaje-Kolstad, G. NMR structure of a lytic polysaccharide monooxygenase provides insight into copper binding, protein dynamics, and substrate interactions. *Proc. Nat. Sci. USA* **2012**, *109*, 18779–18784.
- (34) Courtade, G.; Wimmer, R.; Røhr, Å. K.; Preims, M.; Felice, A. K. G.; Dimarogona, M.; Vaaje-kolstad, G.; Sørlie, M.; Sandgren, M.; Ludwig, R.; Eijsink, V. G. H. Interactions of a fungal lytic polysaccharide monooxygenase with β -glucan substrates and cellobiose dehydrogenase. *Proc. Nat. Acad. Sci. U.S.A.* **2016**, *113*, 5922–5927.
- (35) Peisach, J.; Blumberg, W. E. Structural implications derived from the analysis of electron paramagnetic resonance spectra of natural and artificial copper proteins. *Arch. Biochem. Biophys.* **1974**, *165*, 691–708.
- (36) Meier, K. K.; Jones, S. M.; Kaper, T.; Hansson, H.; Koetsier, M. J.; Karkehabadi, S.; Solomon, E. I.; Sandgren, M.; Kelemen, B. Oxygen Activation by Cu LPMOs in Recalcitrant Carbohydrate Polysaccharide Conversion to Monomer Sugars. *Chem. Rev.* **2018**, *118*, 2593–2635.
- (37) Tandrup, T.; Frandsen, K. E. H.; Johansen, K. S.; J.-G., B.; Lo Leggio, L. Recent insights into lytic polysaccharide monooxygenases (LPMOs). *Biochem. Soc. Trans.* **2018**, *46*, 1431–1447.

- (38) Borisova, A. S.; Isaksen, T.; Dimarogona, M.; Kognole, A. A.; Mathiesen, G.; Várnai, A.; Røhr, Å. s. K.; Payne, C. M.; Sørle, M.; Sandgren, M.; Eijsink, V. G. H. Structural and functional characterization of a lytic polysaccharide monooxygenase with broad substrate specificity. *J. Biol. Chem.* **2015**,
- (39) Frandsen, K. E. H. et al. The molecular basis of polysaccharide cleavage by lytic polysaccharide monooxygenases. *Nat. Chem. Biol.* **2016**, *12*, 298–305.
- (40) Bissaro, B.; Isaksen, I.; Vaaje-kolstad, G.; Eijsink, V. G. H.; Røhr, Å. K. how a lytic polysaccharide monooxygenase binds crystalline chitin. *Biochemistry* **2018**, *57*, 1893–1906.
- (41) Ciano, L.; Paradisi, A.; Hemsworth, G. R.; Tovborg, M.; Davies, G. J.; Walton, P. H. Insights from semi-oriented EPR spectroscopy studies into the interaction of lytic polysaccharide monooxygenases with cellulose. *Dalton Transactions* **2020**, *49*, 3413–3422.
- (42) Simmons, T. J.; Frandsen, K. E. H.; Ciano, L.; Tryfona, T.; Lenfant, N.; Poulsen, J. C.; Wilson, L. F. L.; Tandrup, T.; Tovborg, M.; Schnorr, K.; Johansen, K. S.; Henrisat, B.; Walton, P. H.; Lo Leggio, L.; Dupree, P. Structural and electronic determinants of lytic polysaccharide monooxygenase reactivity on polysaccharide substrates. *Nat. Commun.* **2017**, *8*, 1064.
- (43) Courtade, G.; Ciano, L.; Paradisi, A.; Lindley, P. J.; Forsberg, Z.; Sørle, M.; Wimmer, R.; Davies, G. J.; Eijsink, V. G. H.; Walton, P. H.; Aachmann, F. L. Mechanistic basis of substrate–O₂ coupling within a chitin-active lytic polysaccharide monooxygenase: An integrated NMR/EPR study. *Proc. Natl. Acad. Sci. U.S.A.* **2020**,
- (44) Li, X.; Beeson IV, W. T.; Phillips, C. M.; Marletta, M. A.; Cate, J. H. D. Structural basis for substrate targeting and catalysis by fungal polysaccharide monooxygenases. *Structure* **2012**, *20*, 1051–1061.

- (45) Wu, M.; Beckham, G. T.; Larsson, A. M.; Ishida, T.; Kim, S.; Payne, C. M.; Himmel, M. E.; Crowley, M. F.; Horn, S. J.; Westereng, B.; Igarashi, K.; Samejima, M.; Ståhlberg, J.; Eijssink, V. G. H.; Sandgren, M. Crystal structure and computational characterization of the lytic polysaccharide monooxygenase GH61D from the basidiomycota fungus *Phanerochaete chrysosporium*. *J. Biol. Chem.* **2013**, *288*, 12828–12839.
- (46) Sinnecker, S.; Neese, F. QM/MM calculations with DFT for taking into account protein effects on the EPR and optical spectra of metalloproteins. Plastocyanin as a case study. *Journal of Computational Chemistry* **2006**, *27*, 1463–1475.
- (47) Remenyi, C.; Reviakine, R.; Kaupp, M. Density functional study of EPR Parameters and spin-density distribution of azurin and other blue copper proteins. *J. Phys. Chem. B* **2007**, *111*, 8290–8304.
- (48) Abuznikov, A. V.; Kaupp, M.; Malkin, V. G.; Reviakine, R.; Malkina, O. L. Validation study of meta-GGA functionals and of a model exchange–correlation potential in density functional calculations of EPR parameters. *Phys. Chem. Chem. Phys.* **2002**, *4*, 5467–5474.
- (49) Neese, F. Metal and ligand hyperfine couplings in transition metals complexes: The effect of spin orbit coupling as studied by coupled perturbed Kohn-Sham theory. *J. Chem. Phys.* **2003**, *118*, 3939–2948.
- (50) Kaupp, M., M. Bühl, Malkin, V. G., Eds. *Calculation of NMR and EPR parameters. Theory and applications*; Wiley, 2004.
- (51) Kossmann, S.; Kirchner, B.; Neese, F. Performance of modern Density Functional Theory for the prediction of Hyperfine Coupling structure; meta-GGA and double hybrid functionals. *Mol. Phys.* **2007**, *105*, 2049–2071.

- (52) Remenyi, C.; Reviakine, R.; Abuznikov, A. V.; Vaara, J.; Kaupp, M. Spin-orbit effects on hyperfine coupling tensors in transition metal complexes using hybrid density functionals and accurate spin-orbit operators. *J. Phys. Chem. A* **2004**, *108*, 5026–5033.
- (53) Hedegård, E. D.; Kongsted, J.; Sauer, S. P. A. Optimized basis sets for calculation of electron paramagnetic resonance hyperfine coupling constants: aug-cc-pVTZ-J for the 3d atoms Sc–Zn. *J. Chem. Theory Comput.* **2011**, *7*, 4077–4087.
- (54) Hedegård, E. D.; Kongsted, J.; Sauer, S. P. A. Improving the calculation of electron paramagnetic resonance hyperfine coupling tensors for d-block metals. *Phys. Chem. Chem. Phys.* **2012**, *14*, 10669–10676.
- (55) Hedegård, E. D.; Kongsted, J.; Sauer, S. P. A. Validating and analyzing EPR hyperfine coupling constants with density functional theory. *J. Chem. Theory Comput.* **2013**, *9*, 2380–2388.
- (56) Pedersen, M. N.; Hedegård, E. D.; Kongsted, J. Basis set error estimation for DFT calculations of electronic g-tensors for transition metal complexes. *J. Comput. Chem.* **2014**, *35*, 1809–1814.
- (57) McEvoy, A.; Creutzberg, J.; Kumar Singh, R.; Bjerrum, M. J.; Hedegård, E. The Role of the Active Site Tyrosine in the Mechanism of Lytic Polysaccharide Monooxygenase. 2020; https://chemrxiv.org/articles/preprint/The_Role_of_the_Active_Site_Tyrosine_in_the_Mechanism_of_Lytic_Polysaccharide_Monooxygenase/11994696/1.
- (58) Ahlrichs, R.; Bär, M.; Häser, M.; Horn, H.; Kölmel, C. Electronic structure calculations on workstation computers: The program system Turbomole. *Chem. Phys. Lett.* **1989**, *162*, 165–169.
- (59) Case, D. A. et al. AMBER 14. 2014; University of California, San Francisco.

- (60) Ryde, U. The coordination of the catalytic zinc ion in alcohol dehydrogenase studied by combined quantum-chemical and molecular mechanics calculations. *J. Comput. Aided Mol. Des.* **1996**, *10*, 153–164.
- (61) Ryde, U.; Olsen, M. H. M. Structure, strain, and reorganization energy of blue copper models in the protein. *Int. J. Quantum Chem.* **2001**, *81*, 335–347.
- (62) Tao, J.; Perdew, J. P.; Staroverov, V. N.; Scuseria, G. E. Climbing the density functional ladder: Nonempirical meta-generalized gradient approximation designed for molecules and solids. *Phys. Rev. Lett.* **2003**, *91*, 146401.
- (63) Grimme, S.; Antony, J.; Ehrlich, S.; Krieg, H. A consistent and accurate ab initio parametrization of density functional dispersion correction (DFT-D) for the 94 elements H-Pu. *J. Chem. Phys.* **2010**, *132*, 154104.
- (64) Grimme, S.; Ehrlich, S.; Goerigk, L. Effect of the Damping Function in Dispersion Corrected Density Functional Theory. *J. Comput. Chem.* **2011**, 1456–1465.
- (65) Schäfer, A.; Horn, H.; Ahlrichs, R. Fully optimized contracted Gaussian basis sets for atoms Li to Kr. *J. Chem. Phys.* **1992**, *97*, 2571–2577.
- (66) Eichkorn, K.; Weigend, F.; Treutler, O.; Ahlrichs, R. Auxiliary basis sets for main row atoms and transition metals and their use to approximate Coulomb potentials. *Theor. Chem. Acc.* **1997**, *97*, 119–124.
- (67) Maier, J. A.; Martinez, C.; Kasavajhala, K.; Wickstrom, L.; Hauser, K. E.; Simmerling, C. ff14SB: Improving the accuracy of protein side chain and backbone parameters from ff99SB. *Journal of Chemical Theory and Computation* **2015**, *11*, 3696–3713.
- (68) Jorgensen, W. L.; Chandrasekhar, J.; Madura, J. D. Comparison of simple potential functions for simulating liquid water. *J. Chem. Phys.* **1983**, *79*, 926–935.

- (69) Kirschner, K. N.; Yongye, A. B.; Tschampel, S. M.; González-Outeiriño, J.; Daniels, C. R.; Foley, B. L.; Woods, R. J. GLYCAM06: A generalizable biomolecular force field. Carbohydrates. *J. Comput. Chem.* **2008**, *29*, 622–655.
- (70) Hedegård, E. D.; Ryde, U. Multiscale modelling of lytic polysaccharide monooxygenases. *ACS Omega* **2017**, *2*, 536–545.
- (71) Fritscher, J.; Hrobárik, P.; Kaupp, M. Computational studies of electron paramagnetic resonance parameters for paramagnetic molybdenum complexes. I. Method validation on small and medium-sized systems. *J. Phys. Chem. B* **2007**, *111*, 4616–4629.
- (72) Fritscher, J.; Hrobárik, P.; Kaupp, M. Computational studies of EPR parameters for paramagnetic molybdenum complexes. II. Larger Mo^V systems relevant to molybdenum enzymes. *Inorg. Chem.* **2007**, *46*, 8146.
- (73) Neese, F. The ORCA program system. *Wiley Interdiscip. Rev.: Comput. Mol. Sci.* **2012**, *2*, 73–78.
- (74) Neese, F. Software update: the ORCA program system, version 4.0. *Wiley Interdiscip. Rev.: Comput. Mol. Sci.* **2017**, *8*, e1327.
- (75) Enevoldsen, T.; Oddershede, J.; Sauer, S. P. A. Correlated calculations of indirect nuclear spin-spin coupling constants using second order polarization propagator approximations: SOPPA and SOPPA(CCSD). *Theor. Chem. Acc.* **1998**, *100*, 275–284.
- (76) Sauer, S. P. A.; Raynes, W. T. Unexpected differential sensitivity of nuclear spin-spin coupling constants to bond stretching in BH₄[−], NH₄⁺ and SiH₄. *J. Chem. Phys.* **2000**, *113*, 3121–3129.
- (77) Provasi, P. F.; Aucar, G. A.; Sauer, S. P. A. The effect of lone pairs and electronegativity on the indirect nuclear spin-spin coupling constants in CH₂X (X = CH₂, NH, NH,

- O, S): Ab initio calculations using optimized contracted basis sets. *J. Chem. Phys.* **2001**, *115*, 1324–1334.
- (78) Barone, V.; Provasi, P. F.; Peralta, J. E.; Snyder, J. P.; Sauer, S. P. A.; Contreras, R. H. Substituent effects on scalar ${}^2J({}^{19}\text{F}, {}^{19}\text{F})$ and ${}^3J({}^{19}\text{F}, {}^{19}\text{F})$ NMR couplings: A comparison of SOPPA and DFT methods. *J. Phys. Chem. A* **2003**, *107*, 4748–4754.
- (79) Rusakov, Y. Y.; Krivdin, L. B.; Sauer, S. P. A.; Levanova, E. P.; Levkovskaya, G. G. Structural trends of ${}^{77}\text{Se}$ - ${}^1\text{H}$ spin-spin coupling constants and conformational behavior of 2-substituted selenophenes. *Magn. Reson. Chem.* **2010**, *48*, 633–637.
- (80) Provasi, P. F.; Sauer, S. P. A. Optimized basis sets for the calculation of indirect nuclear spin-spin coupling constants involving the atoms B, Al, Si, P and Cl. *J. Chem. Phys.* **2010**, *133*, 054308.
- (81) Chesnut, D. B.; Moore, K. D. Locally dense basis sets for chemical shift calculations. *J. Comput. Chem.* **1989**, *10*, 648–659.
- (82) Provasi, P. F.; Aucar, G. A.; Sauer, S. P. A. The Use of Locally Dense Basis Sets in the Calculation of Indirect Nuclear Spin-Spin Coupling Constants : The Vicinal Coupling Constants in $\text{H}_3\text{C}-\text{CH}_2\text{X}$ ($\text{X} = \text{H}, \text{F}, \text{Cl}, \text{Br}, \text{I}$). *J. Chem. Phys.* **2000**, *112*, 6201–6208.
- (83) Sanchez, M.; Provasi, P. F.; Aucar, G. A.; Sauer, S. P. A. On the usage of locally dense basis sets in the calculation of NMR indirect nuclear spin-spin coupling constants: Vicinal fluorine-fluorine couplings. *Adv. Quantum Chem.* **2005**, *48*, 161–183.
- (84) Milhøj, B. O.; Hedegård, E. D.; Sauer, S. P. A. On the use of locally dense basis sets in the calculation of epr hyperfine couplings: A study on model systems for bio-inorganic Fe and Co Complexes. *Current Inorganic Chemistry* **2013**, *3*, 270–283.

- (85) Reid, D. M.; Kobayashi, R.; Collins, M. A. Systematic study of locally dense basis sets for NMR shielding constants. *J. Chem. Theory Comput.* **2014**, *10*, 146–152.
- (86) Dunning Jr., T. H. Gaussian basis sets for use in correlated molecular calculations. I. The atoms boron through neon and hydrogen. *J. Chem. Phys.* **1989**, *90*, 1007–1023.
- (87) Kendall, R. A.; Dunning Jr., T. H.; Harrison, R. J. Electron affinities of the first-row atoms revisited. Systematic basis sets and wave functions. *J. Chem. Phys.* **1992**, *96*, 6796–6806.
- (88) Balabanov, N. B.; Peterson, K. A. Systematically convergent basis sets for transition metals. I. All-electron correlation consistent basis sets for the 3d elements Sc–Zn. *J. Chem. Phys.* **2005**, *123*, 64107.
- (89) Weigend, F.; Ahlrichs, R. Balanced basis sets of split valence, triple zeta valence and quadruple zeta valence quality for H to Rn: Design and assessment of accuracy. *Phys. Chem. Chem. Phys.* **2005**, *7*, 3297–3305.
- (90) Becke, A. D. Density-functional exchange-energy approximation with correct asymptotic behavior. *Phys. Rev. A* **1988**, *38*, 3098–3100.
- (91) Lee, C.; Yang, W.; Parr, R. G. Development of the Colle–Salvetti correlation-energy formula into a functional of the electron density. *Phys. Rev. B* **1988**, *37*, 785–789.
- (92) Perdew, J. P.; Burke, K.; Ernzerhof, M. Generalized gradient approximation made simple. *Phys. Rev. Lett.* **1996**, *77*, 3865–3868.
- (93) Becke, A. D. Density-functional thermochemistry. III. The role of exact exchange. *J. Chem. Phys.* **1993**, *98*, 5648–5652.
- (94) Perdew, J. P.; Ernzerhof, M.; Burke, K. Rationale for mixing exact exchange with density functional approximations. *J. Chem. Phys.* **1996**, *105*, 9982–9985.

- (95) Adamo, C.; Barone, V. Toward reliable density functional methods without adjustable parameters: The PBE0 model. *J. Chem. Phys.* **1999**, *110*, 6158–61702.
- (96) Ernzerhof, M.; Scuseria, G. E. Assessment of the Perdew–Burke–Ernzerhof exchange–correlation functional. *J. Chem. Phys.* **1999**, *110*, 5029–5036.
- (97) Kjaergaard, C. H.; Qayyum, M. F.; Wong, S. D.; Xu, F.; Hemsworth, G. R.; Walton, D. J.; Solomon, E. I. Spectroscopic and computational insight into the activation of O₂ by the mononuclear Cu center in polysaccharide monooxygenases. *Proc. Natl. Acad. Sci. USA* **2014**, *111*, 8797–8802.
- (98) Guilleme, J.; San Fabián, J. Basis sets and active space in multiconfigurational self-consistent field calculations of nuclear magnetic resonance spin-spin coupling constants. *J. Chem. Phys.* **1998**, *109*, 8168–8181.
- (99) Helgaker, T.; Jaszuński, M.; Ruud, K.; Górska, A. Basis-set dependence of nuclear spin-spin coupling constants. *Theor. Chem. Acc.* **1998**, *99*, 175–182.
- (100) Peralta, J. E.; Scuseria, G. E.; Cheeseman, J. R.; Frisch, M. J. Basis set dependence of NMR spin-spin couplings in density functional theory calculations: First row and hydrogen atoms. *Chem. Phys. Lett.* **2003**, *375*, 452–458.
- (101) Deng, W.; Cheeseman, J. R.; Frisch, M. J. Calculation of nuclear spin-spin coupling constants of molecules with first and second row atoms in study of basis set dependence. *J. Chem. Theory Comput.* **2006**, *2*, 1028–1037.
- (102) Jensen, F. The basis set convergence of spin-spin coupling constants calculated by density functional methods. *J. Chem. Theory Comput.* **2006**, *2*, 1360–1369.
- (103) Jensen, F. The optimum contraction of basis sets for calculating spin-spin coupling constants. *Theo. Chem. Acc.* **2010**, *126*, 371–382.

- (104) Aggelund, P. A.; Sauer, S. P.; Jensen, F. Development of polarization consistent basis sets for spin-spin coupling constant calculations for the atoms Li, Be, Na, and Mg. *J. Chem. Phys.* **2018**, *149*, 1–10.
- (105) Benedikt, U.; Auer, A. A.; Jensen, F. Optimization of augmentation functions for correlated calculations of spin-spin coupling constants and related properties. *J. Chem. Phys.* **2008**, *129*, 64111.
- (106) Faber, R.; Sauer, S. P. A. On the convergence of the ccJ-pVXZ and pcJ-n basis sets in CCSD calculations of nuclear spin-spin coupling constants: some difficult cases. *Theor. Chem. Acc.* **2018**, *137*, 35.
- (107) Kjær, H.; Sauer, S. P. A. Pople style basis sets for the calculation of NMR spin-spin coupling constants: the 6-31G-J and 6-311G-J basis sets. *J. Chem. Theory Comput.* **2011**, *7*, 4070–4076.

Graphical TOC Entry

TOC FIGURE HERE!

